Research Article Vol. 6, No. 6 / June 2019 / Optica 811

Measurement of ultralow radiation-induced charge densities using picosecond mid-IR laser-induced breakdown

Daniel Woodbury, Robert M. Schwartz, and Howard M. Milchberg*

Institute for Research in Electronics and Applied Physics, University of Maryland, College Park, Maryland 20742, USA
**Corresponding author: milch@umd.edu*

Received 27 March 2019; revised 11 May 2019; accepted 20 May 2019 (Doc. ID 363515); published 20 June 2019

We demonstrate that avalanche ionization breakdown of air with picosecond mid-infrared (mid-IR) laser pulses is an exceptionally sensitive and quantitative probe of extremely low concentrations of charged species. By exponentially increasing the electron density in the vicinity of a single seed atom or molecule to detectable levels, mid-IR electron avalanche is an analogue of single photon detection in photomultiplier tubes and can be useful in a range of applications. We apply the technique to meter-scale standoff detection of a radioactive source, sensitive to extremely low concentrations of radiation-induced negative ions down to $\sim 10^3$ cm^{-3}, limited only by background. By imaging the location of spatially isolated avalanche breakdown sites, we directly measure these low densities and benchmark the performance of standoff detection diagnostics. We discuss implementation of this radiation detection scheme at ranges of 10–100 m and adapting the avalanche probe to detection of other low-density plasmas.

https://doi.org/10.1364/OPTICA.6.000811

1. INTRODUCTION

Assessing the presence of radioactive materials by directly detecting their decay products at large standoff distances is severely limited by geometric divergence and absorption in air. While advanced versions of conventional gamma ray detectors are able to identify and locate radioactive sources up to 100 m [1–3], the R^{-2} decrease in gamma ray flux as source-detector distance R is increased, reduced further by gamma ray absorption, leads to rapid falloff in counts beyond this distance. In addition, these detectors are large and must move to multiple locations to determine the source location. Most schemes for remote detection of radiation therefore rely on probing the local environment near the source, either by deploying remotely controlled or networked sensors [4–8], or by detecting chemical markers of the source with laser-induced-breakdown spectroscopy [9–11], THz spectroscopy [12,13], Raman spectroscopy [14,15], multi- and hyperspectral imaging [16], or Fourier transform infrared (IR) spectroscopy [17]. However, these optical methods require an unobstructed line-of-sight view of trace amounts of the radioactive substance outside any shielding, and thus could be defeated by careful source handling and cleaning of container surfaces.

Rather than relying on chemical traces of the source material itself, several recent approaches aim to detect the elevated levels of free electrons and negative ions in the air near a shielded radioactive source using a laser-driven electron avalanche [18,19]. The concentration of these radiation-induced charged species is far too low for direct detection, with densities in the approximate ranges $\sim 10^{-2}$–10^{1} cm^{-3} for electrons and $\sim 10^{4}$–10^{7} cm^{-3} for ions [20]. However, the use of laser-driven avalanche breakdown, which starts from a single electron and exponentially increases the electron density to detectable levels, can be viewed as an analogue of the detection of single photons by a photomultiplier tube.

Electron avalanche ionization is initiated when the seed electrons are heated collisionally by intense electromagnetic wave-driven elastic collisions with background neutrals, converting coherent oscillatory electron motion into random velocities, or heating. Once electrons gain sufficient energy, they can liberate additional electrons through inelastic ionizing collisions with air molecules. If the laser-induced heating is sufficient to overcome losses such as electron cooling, attachment, and diffusion, the electron density will increase exponentially until it saturates [21]. In the case of an avalanche-based detection scheme, the initial free electrons are generated by the ionization of air by decay products of radioactive sources.

The earliest detection concept based on avalanche ionization envisioned the use of a mm-wave or THz source to drive the breakdown seeded by free electrons in the vicinity of the radioactive material [18], and was the subject of simulation work [22–24] and a recent experiment [25]. Given the limited practicality and availability of high-power mm-wave and THz sources, other proposals and experiments examined the use of visible and near-IR laser drivers, but this wavelength range is limited by the deleterious competing effect of multiphoton ionization (MPI) [26], which generates a population of free electrons early in

the laser pulse that overwhelms the seed population induced by the radioactive source.

Recently, we demonstrated that a 50 ps FWHM laser pulse in the mid-IR wavelength range ($\lambda = 3.9$ μm, photon energy ~0.3 eV) is exceptionally well suited as an avalanche driver for radioactive source detection [21]. Free electrons, liberated by interaction of source decay products with air, quickly attach to oxygen to form O_2^- ions, with a bond energy of ~0.45 eV, which then forms the basis of subsequent air chemistry [19,20,27]. Early in the mid-IR pulse, the electrons are re-liberated by the high rate of two-photon ionization of O_2^-, and then seed a subsequent avalanche. A variable initial density of O_2^- ions, determined by the activity and location of the radioactive source, introduces a commensurate temporal shift in the onset of breakdown [21], defined in that work as the time when there is detectable attenuation of a *co-propagating* chirped, near-IR probe pulse. Measurement of these breakdown shifts enabled estimates of O_2^- density and, in turn, the local radiation environment [21]. An important point is that for a 50 ps laser driver and initial seed densities $< \sim 10^{10}$ cm^{-3}, avalanche breakdown sites seeded by single seed charges remain isolated owing to very limited electron diffusion during the pulse [21,28].

In this paper, we extend the mid-IR avalanche technique to detect radiation at longer standoff distances, using a chirped mid-IR pump pulse, and spectrally resolved backscatter detection enabled by a single-shot, high-sensitivity mid-IR spectrometer. Backscatter detection of the pump supplants the co-propagating probe detection of our previous work [21]. Additionally, by imaging and counting individual breakdowns in the laser focal volume, we directly determine the density of negative ion seeds (primarily O_2^-) down to ~10^3 cm^{-3}, limited by breakdowns likely seeded by dust. These densities are well below those first estimated in our previous paper. Directly counting breakdowns allows absolute benchmarking of three diagnostics employed here for remote detection. More generally, it enables measurement of transient, ultralow electron densities far below those measurable through other techniques such as microwave [29] or optical probing [30], or plasma conductivity measurements [31].

The paper is organized as follows. In Section 2, we present the performance of three standoff diagnostics of low levels of radioactive source-induced air ionization, benchmarked by absolute densities measured through direct imaging of breakdown plasmas. In Section 3, we discuss our ability to measure the presence of a single charge via the avalanche it seeds, and present numerical simulations of the avalanche breakdowns. In Section 4, we discuss scaling to longer standoff distances, as well as other applications for measuring ultralow charge densities.

2. EXPERIMENTAL RESULTS AND DISCUSSION

A. Setup and Diagnostics

Experiments were performed with chirped, high-energy mid-IR laser pulses (50 ps FWHM, super-Gaussian temporal profile, 15–35 mJ, $\lambda = 3.6$–4.2 μm, 20 Hz repetition rate, 4% pulse-to-pulse energy fluctuations) [21,32], which were focused by a 1 m spherical mirror [see Fig. 1(a)] to a FWHM focal spot of ~140 μm as measured by an InSb camera. We note that the beam was focused at $f/33$ (3 cm beam focused with a 1 m mirror), giving a Rayleigh range of ~5 mm, but that aberrations on the beam produced a focal spot larger than the ~100 μm spot expected for Gaussian focusing. The focal spot changed slightly as pulse energy was increased, resulting in peak intensities ranging from 1.5 to 3×10^{12} W/cm^2 (1.5–3 TW/cm^2). The pulses are generated in an optical parametric chirped pulse amplifier (OPCPA) system, which can produce ultrashort (87 fs) pulses, but in the current experiment, we bypass the final grating

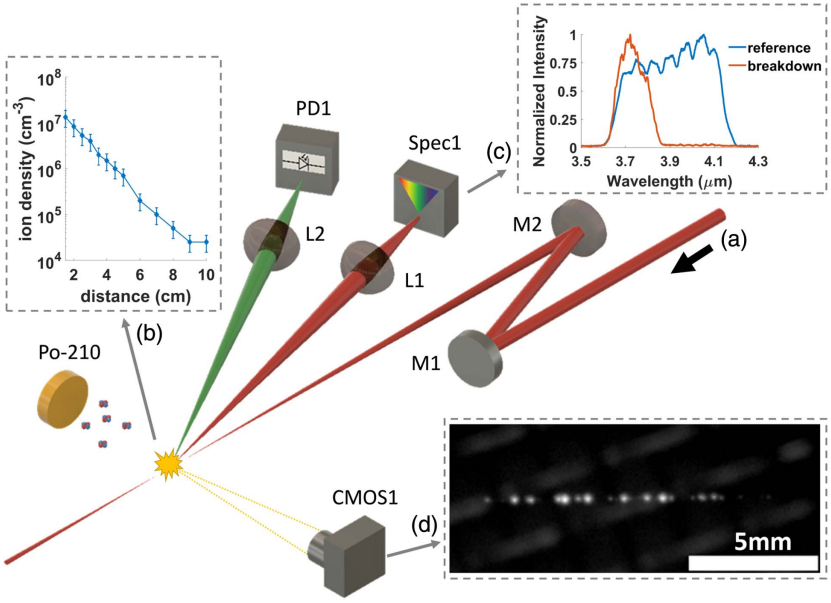

Fig. 1. Experimental setup. (a) A chirped, 50 ps (FWHM) $\lambda = 3.6$–4.2 μm laser pulse is focused by a 1 m focusing mirror, M2, to a focal spot near a 5 mCi Po-210 source emitting 5.3 MeV α-particles, driving electron avalanche. (b) O_2^- ions formed in the vicinity of the α-source provide seed electrons for the avalanche, with total negative ion concentration versus distance from the α-source shown in the plot. (c) Backscattered mid-IR light is collected by lens L1, located 1 m from the breakdown, into a home-built mid-IR imaging spectrometer, Spec1, with a sample backscatter spectrum and reference laser spectrum shown. Visible plasma emission is collected by lens L2 onto an amplified silicon photodiode PD1. A notch filter rejected stray light from the 1064 nm OPCPA pump laser. (d) Plasma emission from the breakdown is also imaged onto camera CMOS1, with a sample image shown.

compressor to maintain a 50 ps FWHM, positively chirped pulse. The laser-driven avalanches were monitored by three "field" diagnostics that one might use in a practical radioactive source detection scenario, plus a benchmark diagnostic used to understand the behavior of the field diagnostics. The field diagnostics are backscattered spectra of the chirped pump pulse, relative backscattered pump energy, and collection of the visible breakdown plasma emission. The benchmark diagnostic is the direct imaging of the full breakdown volume. All these measurements are described in more detail below.

The focused pulses drive avalanche breakdowns at a 20 Hz repetition rate in ambient air irradiated by a 5 mCi Po-210 spot source emitting 5.3 MeV α-particles (NRD Nuclespot). The distance between the source and the laser focus, d_{s-f}, is varied by translating the source on a rail. To prevent ions from a previous breakdown plasma seeding a successive avalanche, dry air is flowed at ~60 cm/s across the focal region. The steady state negative ion density induced in air by the Po-210 source is measured using a Gerdien condenser ion counter (AlphaLab), with a plot of density versus distance from the source shown in Fig. 1(b). The minimum distance of ~1 cm is set by the ion counter geometry. A mechanical shutter capable of blocking all α-particles is affixed to the source for a portion of experimental runs to demonstrate on–off responses to radioactivity. Pump light backscattered from the breakdown plasma is collected at ~$f/80$ at 12° from the laser axis by a lens (L1) located 1 m from the plasma, and directed into a single-shot mid-IR imaging spectrometer (Spec1) with a liquid nitrogen cooled InSb camera (IRCameras IRC806) in its image plane. This unique diagnostic is used to measure the avalanche onset delay and the relative amount of backscattered mid-IR pump energy. It is able to capture single-shot backscatter spectra and is far more sensitive than spectrometers based on a PbSe array. Examples of the incident positively chirped pump spectrum and the spectrum backscattered from an avalanche breakdown are shown in Fig. 1(c). Visible line and continuum emission (300–1000 nm) from the breakdown plasma is collected at $f/18$ at 16° from the laser axis by a lens (L2) located 90 cm away from the plasma and focused onto an amplified Si photodiode (PD1, Thorlabs PDA100A2). Images of the plasma emission in the breakdown volume are also collected at 90° from the laser axis by a low noise CMOS camera (CMOS1, Thorlabs Quantalux), with an example image shown in Fig. 1(d).

B. Avalanche Seed Formation, Detachment

As explained in [21], α-particles generate excess ionization, leading to the creation of O_2^- ions and other radiation-induced species. A simple model [20,21] suggests that total ion counts should be ~10^8 cm^{-3} < ~3 cm from the 5 mCi source and ~10^4 cm^{-3} at background conditions (see Supplement 1). With the Gerdien condenser ion counter, we measure total negative ion densities from ~10^7 cm^{-3} down to ~10^4 cm^{-3} moving 10 cm away from the α-source, as shown in Fig. 1(b). With the α-source blocked, the ion counter measures background ion densities ~10^2–10^3 cm^{-3}. We note that the ion counter cannot distinguish among different species of negative ions, and it has a ~1 cm wide intake port fed by weak fan-driven air flow that will smear out any ion density gradients present. As such, we use the ion counter measurements as an estimate of the trends in total seed ion density; we argue below that the O_2^- ions are only a fraction of these counts.

In the focal volume, O_2^- ions, with a binding energy of 0.45 eV, are detached early in the mid-IR pulse via two-photon ionization [33], providing a seed source for subsequent electron avalanches. Neutral atoms and molecules are not significantly ionized by the mid-IR pulse; MPI of O_2, which requires 38 photons at $\lambda = 3.9$ μm, is an extremely low probability process [21]. The more tightly bound negative ions produced through air chemistry (NO_3^-, NO_2^-, O_3^-, O^- and OH^-) [34,35], which have binding energies of 1.5–4 eV [36], will also experience much lower rates of photoionization early in the pulse, such that avalanches are likely mainly seeded by O_2^-. In contrast, our previous work using a near-IR laser ($\lambda = 0.8$ μm) found that 8-photon MPI of neutral O_2 generated a seed density that overwhelmed that generated by the radioactive source, making $\lambda = 0.8$ μm laser-driven avalanches insensitive to the presence of the source [26].

C. Plasma Evolution and Detection

Once seed electrons are present in the laser focal volume, avalanche breakdown can proceed only if the local laser intensity exceeds a threshold above which electron attachment, diffusion, and inelastic collision losses are overcome. A finite laser pulse duration increases the effective threshold significantly beyond what it would be for a CW beam, since the growth rate must increase in order to drive a detectable breakdown *before* the end of the pulse. In the limit of very short pulses, the breakdown threshold that leads to a detectable breakdown is approximately $I_b(\mathrm{TW/cm^2}) \sim 8 \times 10^2 / P\tau\lambda^2$, where P is the pressure (atm) and τ is the pulse length (ps) [37], giving $I_{\mathrm{th}} \approx 1$ TW/cm^2 for our conditions. Exposed to this intensity or greater, individual free electrons initiate an avalanche that reaches a significant fraction of the laser critical density ($N_{\mathrm{cr}} = 7.2 \times 10^{19}$ cm^{-3} at $\lambda = 3.9$ μm) before the end of the pulse. Pump absorption and plasma heating then dramatically increase, leading to increased backscatter of the pump pulse and a strong, visible spark.

Breakdown timing is correlated with both peak intensity and seed density. As the peak intensity increases, the volume where the intensity exceeds the breakdown threshold increases, increasing the probability that an electron will be liberated from an ion and initiate an avalanche. As seed density increases, these liberated electrons are more likely to occupy regions of high intensity, leading to a higher local temperature, an increased collisional ionization rate, and a faster breakdown. Since the pump pulse is positively chirped, providing a frequency-to-time map, the air breakdown evolution is encoded in its backscatter spectrum. We define the breakdown onset time by locating the longest wavelength whose amplitude in the backscattered spectrum is above the spectrometer detector's noise floor. Backscatter from a seed-initiated breakdown is detectable on the mid-IR spectrometer when the local electron density reaches ~10^{18} cm^{-3}, based on considerations of plasma size and detector sensitivity. The breakdown onset time is then converted to breakdown time advance, defined to be the time interval between the onset time and the end of the pulse. For details on the wavelength-time mapping, detection threshold estimate, and spectrum data processing, see Supplement 1.

D. On–Off Measurements

Avalanche breakdowns were detectable (signal-to-noise ratio, SNR > 1) in backscatter diagnostics for peak intensities above a threshold of ~1.5 TW/cm^2, in agreement with the estimate

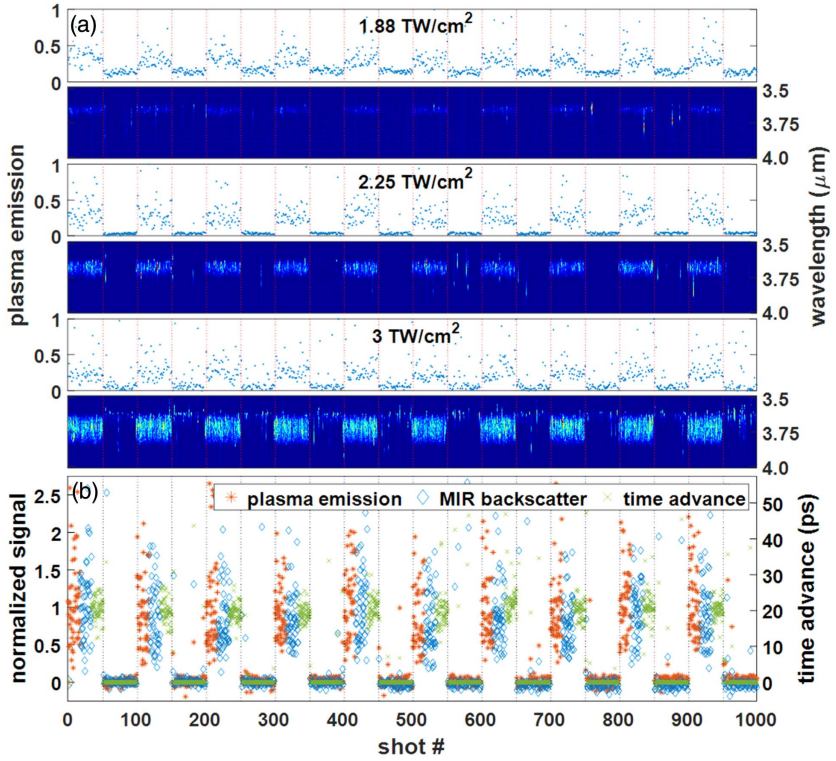

Fig. 2. Real-time measurements of radiation with data collected at 10 Hz (rate limited by data acquisition speed). (a) Single-shot measurements of plasma emission and mid-IR backscattered spectra from the laser focus 2 cm from the α-source, with a shutter blocking/unblocking the radiation every 50 shots. For each intensity, the visible plasma emission is shown on the top panel, while spectra are shown on the bottom panel. (b) All three diagnostic signals plotted together for pump intensity of 2.25 TW/cm^2. For each data point, we subtract the median background (non-irradiated) signal and divide by the median irradiated response in order to directly compare the variation of each diagnostic. In order to compare the data scatter for the three channels on unblocked shots, the plot artificially reorders the shot numbers and squeezes 50 shots for each detection channel into adjacent ∼13 shot-wide intervals.

above. We first show in Fig. 2 the effect of opening and closing the radioactive source shutter. Plotted are the signals from our breakdown diagnostics for 1000 consecutive laser shots, with the shutter opening and closing every 50 shots. The laser focus is 2 cm from the source, with the beam propagating perpendicular to the source normal direction, as depicted in Fig. 1. Examining the plots of pump backscattered spectra [bottom panels of Fig. 2(a)], it is seen that as the peak laser intensity increases, earlier breakdown is manifested as the appearance of redder portions of the positively chirped pump spectrum. For a few shots at every intensity (∼2%–3% of all shots in the experiment), a single, very bright breakdown site (∼5 × brighter than other breakdowns, as imaged by the CMOS1 camera) develops very early in the pulse (25–40 ps time advance), likely due to random seeding by dust in the focal volume, as explained further in Supplement 1. As intensity is further increased to 3 TW/cm^2, breakdown occurs intermittently in non-irradiated air (with shutter closed), due to seeding by the background concentration of O_2^- ions, or by enhanced seeding from other ions, as discussed below. Comparing the backscatter energy, plasma emission, and breakdown time advance signals on one plot, Fig. 2(b) shows the on–off response at 2.25 TW/cm^2, where each point is rescaled by subtracting the median background (non-irradiated) response and then dividing by the median irradiated response. The left scale is normalized backscattered energy and breakdown plasma emission, and the right scale is breakdown time advance. The plot is truncated at 3× median values. We use the median rather than the mean for rescaling to avoid skewing by the breakdowns seeded by dust. The plot shows that the total backscattered mid-IR signal and plasma emission exhibit more shot-to-shot variability (with standard deviations of 42% and 52% of the median value after excluding high scatter points) than the breakdown time advance (with a standard deviation of 21% of the median value).

Since the seed ion density 2 cm from the source is high enough for a large number of breakdown sites in the threshold volume (with some located at the highest intensity) such that the time advance is expected to be constant shot to shot, the different spreads in the three breakdown signals reflect their consistency as diagnostics of the seed ion density. For integrated mid-IR backscatter, the increased variability stems from propagation through randomly placed plasma sites: varying shot-to-shot backscatter interference between multiple scattering points in the breakdown volume, evident as fluctuating spectral fringes in the backscatter spectrum. These shot-to-shot fluctuations are increased by fluctuations in the shape and local density distribution of plasma. Likewise, the relationship between laser energy and plasma heating (and plasma emission), already nonlinear in the case of a uniform plasma, is also subject to local propagation effects: large shot-to-shot variations from scattering and refraction of the laser pulse from local plasma non-uniformities. The observed time advance, on the other hand, is largely decoupled from propagation in the vicinity of high-density plasma: it is determined only by a single seed ion site near the region of highest intensity that breaks down the earliest, with the spectral content associated with that early backscatter unaffected by the interference and spectral fringing from the later backscattering from avalanche sites located

in regions of lower pump intensity, which begin sizeable backscatter at later times.

E. Seed Ion Density Scan

To compare the behavior of our avalanche signals over a range of radiation-induced seed densities, we scanned the α-source-laser focus separation $d_{s\text{-}f}$ over 1–9 cm while keeping the intensity fixed. Figures 3(a)–3(c) present the raw data from our three detection channels for a peak laser intensity of 2.25 TW/cm^2, while Fig. 3(d) plots the mean and standard deviation of the measurements, again scaled between the maximum values of each detection channel and background.

As seen in Fig. 3(d), while the decreasing responses of the three detection channels are similar far from the source, near the source, the response of the breakdown time advance channel is strikingly different from the other two. The breakdown time advance is roughly constant near the source because a seed ion is highly likely to be present near the region of highest intensity. For $d_{s\text{-}f}$ beyond ~3 cm, the time advance decreases and becomes more variable, since only a few seed ions will be randomly distributed within the focal volume. Far from the source ($d_{s\text{-}f}$ = 5–9 cm), most shots do not record a breakdown advance (time advance = 0), but those that do exhibit an advance that continues to decrease with $d_{s\text{-}f}$.

The backscattered pump energy and visible plasma emission, on the other hand, start at low levels near the source and then rise quickly to the peak near ~3 cm, falling to lower levels beyond that point. The lower levels of these signals near the source do not reflect an actual decrease in seed ion density, but rather the effect of pump laser scattering from multiple localized high-density-breakdown plasmas, as discussed below.

F. Breakdown Imaging

Under all conditions of our experiments, breakdowns consisted of discrete, countable avalanche sites. Individual seed ion locations in the focal volume were directly counted by imaging plasma emission from their associated avalanche sites (using camera CMOS1, as shown in Fig. 1(d), which shows a sample image). This enabled benchmarking of our three breakdown diagnostics using absolute seed ion counts. Collected images were processed to count breakdown sites and record the brightness of each one. A summary is presented in Fig. 4, showing in panel (a) the mean number of breakdown sites at each laser intensity and α-source-laser focus separation, $d_{s\text{-}f}$, averaged over 500 shots. Overlaid for reference is the ion density curve from Fig. 1(b), rescaled for plotting here. To calculate a seed density from these counts, we must first find the volume for which the breakdown threshold is exceeded. For a Gaussian beam of peak intensity I exceeding a breakdown threshold I_{th} and focused to a spot radius w_0, the total volume for which $I > I_{\text{th}}$ is

$$V_{\text{th}} = \frac{\pi^2}{3}\frac{w_0^4}{\lambda}\left[\frac{2}{3}(5+\hat{I})\sqrt{\hat{I}-1} - 4\tan^{-1}\left(\sqrt{\hat{I}-1}\right)\right], \quad (1)$$

where $\hat{I} = I/I_{\text{th}}$ [38]. Thus, the number of breakdown sites $= N_i V_{\text{th}}$, where N_i is the seed density, will increase with seed ion density and/or intensity. The images bear out this trend, as the average number of breakdown sites increases both as the source is moved closer to the focal volume (higher ion density) and as peak intensity is increased. At a given $d_{s\text{-}f}$, (and corresponding seed density), the breakdown count scales as $n \propto V_{\text{th}}(\hat{I})$. Fitting the measured breakdown counts (at $d_{s\text{-}f}$ = 1 cm) to $V_{\text{th}}(\hat{I})$, using I_{th} as a fitting parameter, gives I_{th} ~1.1 TW/cm^2, a value in line with similar fits at other values of $d_{s\text{-}f}$ up to 4 cm (which give I_{th} = 0.9–1.3 TW/cm^2). This lower breakdown threshold (compared to backscatter diagnostics) is consistent with plasma imaging being able to detect much lower plasma densities due to its higher collection efficiency.

Over the range of intensities in Fig. 4, the volume for which $I > I_{\text{th}}$ is in the range V_{th} 2.7×10^{-5} to 2.7×10^{-4} cm^{-3}. This gives a peak O_2^- ion density ranging from $2(^{+2}_{-1})10^5$ cm^{-3} at $d_{s\text{-}f}$ = 2.5 cm to ~10^4 cm^{-3} at $d_{s\text{-}f}$ = 4 cm. Comparison with the ion counter measurements, which peak at 10^7 cm^{-3} near the source, shows that the seed ion count is only a fraction of the number of negative ions detected by the Gerdien counter,

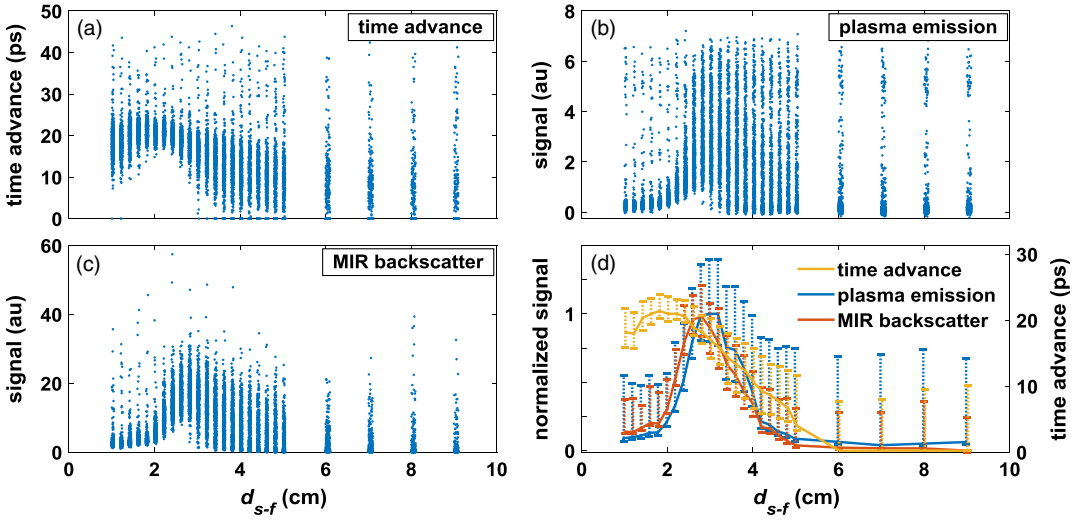

Fig. 3. Single-shot measurements of (a) time advance, (b) plasma emission, and (c) total MIR backscatter for a pump intensity of 2.25 TW/cm^2 as the distance from the α-source, $d_{s\text{-}f}$, is scanned over 1–9 cm. 500 shots were taken at each position, with 2 mm increments up to 5 cm, and 1 cm increments thereafter. The minimum $d_{s\text{-}f}$ of 1 cm is limited by the Po-210 source holder. (d) Mean values at each location, with error bars denoting the standard deviation of data (calculated separately for values above and below the mean). As discussed later in the text, the suppression in plasma emission and total backscatter is caused by scattering losses at high seed densities.

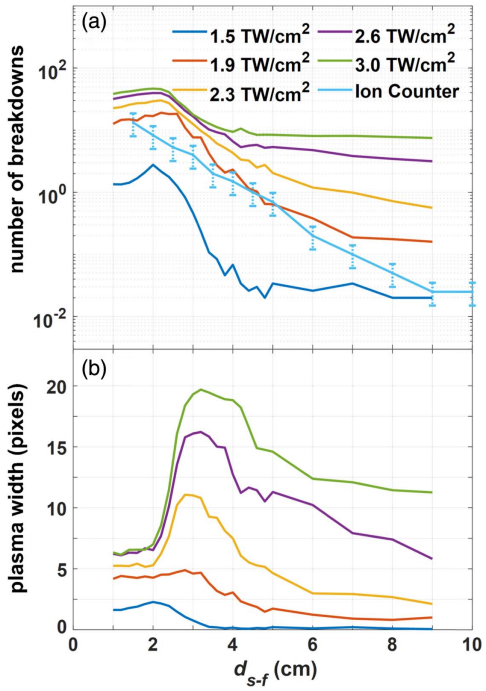

Fig. 4. Summary of data from CMOS camera images. (a) Mean number of individual breakdowns observed for a range of intensities as function of source distance, with 500 shots at each position. Figure 1(d) shows a typical image from which breakdowns were counted. The ion density measured with the Gerdien ion counter is overlaid with arbitrary scaling for comparison. (b) Mean value of the widest peak extracted from each shot (over 500 shots) for the same scan of intensity and source distance. Each camera pixel corresponds to ∼50 μms, such that many smaller breakdowns lead to detection on a single pixel.

although the seed ion density does track the total negative ion density. This behavior is consistent with the weakly bound O_2^- ions being part of a complex air chemistry chain that ends in more chemically stable terminal ions [34,35].

The plots of breakdown site counts versus d_{s-f} in Fig. 4(a) show a peak seed ion density near ∼2–2.2 cm. We identify this as the location of the Bragg peak for 5.3 MeV α-particles in air, which is consistent with continuous slowing down approximation (CSDA) calculations of their stopping distances (∼3.5 cm) [39], but is lower due to energy lost as α-particles leave the source material, and their angular emission spreads from the source foil. At the Bragg peak, α-particle energy deposition in air increases the particles near the end of their range. This results in a peak in ion density near d_{s-f} ∼2–2.2 cm followed by a rapid drop at longer distances, which is borne out in all curves in Fig. 4(a). This feature also agrees with the decrease in observed breakdown time advance seen beyond 2.5 cm in Fig. 3(d), and in our previous work [21]. The absence, in the overlaid Gerdien ion counter curve in Fig. 4(a), of a peak ion density near 2 cm, suggests that the ion counter measurements were smeared out by air flow and the size of the intake port.

Farther from the source (d_{s-f}>5 cm), the number of breakdown sites in the focal volume plateaus, and problematically, the seed ion densities calculated using V_{th} are intensity dependent. There are several factors contributing to this effect. First, 2%–3% of all shots show early breakdowns, likely seeded by dust, which introduces a baseline average of ∼0.02 breakdown sites per shot, as seen in the curve at 1.5 TW/cm^2. Dividing the remaining four curves by the breakdown volume $V_{th}(\hat{I})$ shows an increase in the seed ion density as $N_i \propto I^{4-5}$. We speculate that this increase is characteristic of MPI of other, more tightly bound ions (NO_3^-, NO_2^-, O_3^-, OH^- and O^-, which require 13, 8, 7, 6 and 5 pump photons to ionize, respectively [36]), which result from air chemistry evolution beginning with the O_2^- seed ions. Since α-particles do not appreciably ionize air past their stopping range of ∼3.5 cm, the ions present at d_{s-f}>5 cm travel by air flow or diffusion, which allows time for the evolution of these additional ion species. Since these ions have a higher ionization potential, they ionize later in the pulse, leading to sites of delayed breakdown that are imaged by the camera but do not change the time advance.

To assess the importance of propagation effects on our three detection channels, we examined the laser energy absorbed at local breakdown sites. We recorded the FWHM width of the brightest breakdown site in each image, which, assuming saturation of the local breakdown plasma density, correlates with the laser energy absorbed by that plasma and its backscatter over the pulse. This metric, averaged over 500 shots at each position, is shown in Fig. 4(b), with each pixel value corresponding to ∼50 μm. It is seen that for $I > 1.9$ TW/cm^2, the breakdown sites with greatest heating are located near $d_{s-f} \sim 3$ cm. However, for $d_{s-f} < 3$ cm, the maximum plasma size (and heating) drops abruptly and clamps at ∼5 pixels (250 μms), irrespective of intensity. This behavior is not due to the reduced ion density before the Bragg peak, since Fig. 4(a) shows that the ion density close to the source (<2 cm) is still higher than beyond 3 cm, yet breakdown sites for $d_{s-f} > 3$ cm are more strongly heated. The decrease in plasma size is less pronounced for the runs at 1.9 TW/cm^2, where the breakdown count in the focal volume is ∼10, compared to 20–50 breakdowns at higher intensities. For $I = 1.5$ TW/cm^2 on the other hand (breakdown count ∼1–2), the peak heating occurs at the same position as the Bragg peak (∼2 cm), consistent with the highest seed ion density giving the highest probability of seed locations close to peak laser intensity.

We infer from these results that scattering and refraction from multiple plasma sites dominate our laser-driven avalanches at high laser intensity and seed ion density. As the number of breakdown sites increases, Mie scattering from plasmas upstream of the focused beam waist can reduce the intensity of the laser pulse, limiting late time heating and growth of downstream breakdowns. A simplistic model that overestimates this effect takes each avalanche site as a plasma sphere of diameter 250 μm [based on the clamped plasma size in Fig. 4(b)], which casts a shadow over half the longitudinal extent of the breakdown volume (∼3 mm). This predicts an occluded volume (shadow) per seed ion of $\sim 10^{-4}$ cm^3. Hence, for seed ion densities $> \sim 10^4$ cm^{-3}, the heated and expanding breakdown sites scatter the pump laser enough to mutually limit their heating—hence the effective clamping in plasma heating and growth observed at short distances in Fig. 3(b). Despite the simplicity of this model, this estimate is within an order of magnitude of the measured seed ion concentration of $\sim 10^5$ cm^{-3} at 3 cm, where these effects are important. Since the plasma breakdowns affect pump propagation only toward the end of the plasma evolution when the density and size are high enough to induce significant scattering and refraction,

this effect should not affect the *number* of breakdown locations plotted in Fig. 4(a), but does limit the late time heating, plasma size, and subsequent laser backscatter and plasma emission. This then explains the divergence in backscatter and plasma emission signals versus the time advance signal in Fig. 3: time advance is determined by breakdowns occurring sufficiently early enough that propagation effects have not yet affected the signal, while integrated backscatter and plasma emission sample the breakdowns through the full pulse, and so both are strongly affected by propagation effects.

While a complete treatment of 3D optical propagation through a time-dependent distribution of high-density plasma scattering centers is beyond the scope of this work, we note that prior work has often observed that scattering from laser-produced plasma limits plasma heating and growth further downstream [40,41]. In addition, carbon black suspensions that seeded localized electron avalanche were observed to limit the laser intensity through Mie scattering [42], consistent with our observation of the clamping of plasma heating and growth near the α-source, as plotted in Fig. 4(b).

3. THEORETICAL EXPLANATION AND SIMULATIONS

A. Ionization Simulation Models

In the present experiment using 50 ps laser pulses, avalanche breakdown sites seeded by individual ions are nearly stationary and evolve entirely according to the local laser intensity. Because electrons are liberated from seed ions very early in the laser pulse [21], the theory presented here considers free electron seeds only. After a time t, electrons in a tenuous plasma would diffuse over a length scale $l_d = \sqrt{2D_e t}$ for an electron diffusion coefficient $D_e = k_B T_e/m\nu$, where ν is the electron-neutral collision rate, m is the electron mass, k_B is Boltzmann's constant, and T_e is the electron temperature. Using typical values from our breakdown simulations (below) of $k_B T_e \sim 10$ eV and $\nu \sim 3 \times 10^{12}$ s^{-1} [20,43] gives $l_d \sim 3$–8 μm for time delays $t \sim$ 10–70 ps during the heating pulse envelope. This length is an overestimate that applies to electrons very early in the breakdown before they are restrained by local plasma electrostatic forces. The small value of l_d guarantees that individual breakdown sites remain localized and stationary relative to the scale of the laser focus, where the spot diameter and confocal parameter are $2w_0 =$ 240 μm and $2z_0 = 10$ mm.

The above considerations restrict the type of ionization model appropriate for our conditions. Zero-dimensional (0D) models—ionization rate equations with no spatial dependence of ion or electron densities—implicitly assume that these densities are uniform or smoothly varying [19,20]. Given an initial seed density, such a model gives a specific avalanche onset time; the model is deterministic and predicts a specific reduction in the number of generations of electron growth needed to reach saturation [19,20,25]. However, 0D models begin to be appropriate only at sufficiently large initial seed ion densities—an estimate of which is $N_i > l_d^{-3} \sim 10^{11}$ cm^{-3}, orders of magnitude higher than our measured seed ion counts. Under our conditions, the time to saturation is *non-deterministic*: it depends on where, statistically, single seeds are located in the laser focal volume.

We can, however, use a 0D model to provide the local electron density growth rate and electron temperature and apply it to the breakdown proceeding from a single discrete seed electron. We use the 0D avalanche model presented in our prior work, which adiabatically follows the laser intensity (see Supplement 1), but have updated it to include corrections to loss rates and the collisional ionization rate at high electron temperatures [44,45]. Using these growth rates, we then track the local density used in a simulation of a single electron seed by dividing the number of electrons by an effective volume $\frac{4}{3}\pi l_d^3$, where l_d transitions to an ambipolar diffusion scale length once the plasma Debye length is equal to the electron diffusion length [28,43].

The breakdown onset time for a seed electron exposed to a given peak intensity is taken to be the time when the electron density reaches $\sim 10^{18}$ cm^{-3}, which corresponds to the experimental breakdown detection threshold (see Supplement 1). The resulting time advance (the difference between the breakdown time and the end of the pulse) for a range of local peak intensities is shown in Fig. 5(a) for a third-order super-Gaussian pulse with FWHM duration of 50 ps, which matches the measured temporal profile of our pulse. The simulation curve in Fig. 5(a) predicts a breakdown onset intensity threshold $\sim$1.6 TW/cm^2, which agrees well with the experimental threshold of $\sim$1.5 TW/cm^2 for observing backscatter. Maximum time

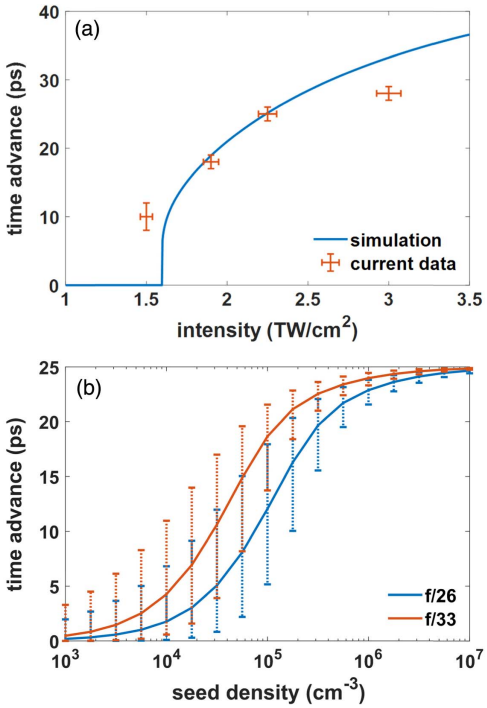

Fig. 5. Results from numerical simulations. (a) Simulated breakdown time advance (as determined by reaching a threshold electron density of 10^{18} cm^{-3}) for single electrons exposed to a super-Gaussian temporal pulse for a given local peak intensity. Below the threshold of $\sim$1.6 TW/cm^2, the model predicts no detectable breakdown. Maximum time advance versus intensity is also plotted for current experimental data. (b) Statistical breakdown time advance modeled for two focal volumes for peak intensity 2.25 TW/cm^2 as a function of seed density. Each point shows the mean expected breakdown time and spread, calculated (separately) as the standard deviation for values above and below the mean. For the larger focal spot ($f/33$), the volume above the breakdown threshold [Eq. (1)] becomes larger, providing sensitivity to a lower seed density.

advances observed in the experiment are also plotted, and show reasonable agreement with simulations.

B. Statistical Determination of Breakdown Onset Time

While our repurposed 0D model predicts the breakdown time advance initiated by a seed electron exposed to a given intensity, the distribution of seed electrons in a region of spatially varying intensity introduces a statistical spread in the onsets of local breakdowns. For a seed electron density N_i, the average number of seed electrons in this breakdown volume is $n = N_i V_{\mathrm{th}}$, where V_{th} is the breakdown volume in Eq. (1). For $n \ll 1$, there will rarely be a breakdown, while for $n \gg 1$, there is a high probability of finding an electron in the region of highest intensity, leading to a near-deterministic breakdown time advance corresponding to the peak intensity. For intermediate densities, a range of breakdown times will be observed for random placement of the ions in the laser focal volume at a range of local intensities. The Poisson probability that a given intensity I will determine the time advance is $P(I) = e^{-n'}(1 - e^{-\delta n})$, where $\delta n = N_i \delta V$ is the average number of seed electrons in a volume element δV corresponding to intensity I, and $n' = N_i V'$, where V' is the volume corresponding to higher intensity $I' > I$ [21]. A calculation incorporating these probabilities is presented in Fig. 5(b), which tracks the mean value of breakdown time advance for different focal volumes as seed density is increased (at constant peak intensity of 2.25 TW/cm^2). Error bars are given by the standard deviation above and below the mean. It is seen that increasing the f/number (and focal volume) shifts the sensitivity to lower seed densities, and that at high seed densities, the time advance saturates to the values predicted in Fig. 5(a). The simulation results are in good quantitative agreement with our present experiment ($f/33$ focusing, or 3 cm beam focused at 1 m): at 2.5 cm from the source where we measured a seed density $2(^{+2}_{-1}) \times 10^5$ cm^{-3} through imaging, we measured a time advance (for 2.25 TW/cm^2) ranging from 19–22 ps [range of standard deviation error bars in Fig. 3(d)], matching the range generated through simulations (18–23 ps at a seed density of 1.7×10^5 cm^{-3}). At $d_{s\text{-}f} = 4$ cm (seed density $\sim 10^4$ cm^{-3}), we measured a time advance of 6–15 ps, compared with a simulated time advance of 0.5–10 ps.

The agreement between simulations and experiment, particularly with the benchmarking provided by imaging individual breakdown sites, provides confidence that our detection method can accurately assess low ion concentrations through measurements of the avalanche time advance. Since the time advance is inherently statistical, many shots are required to assess the ion concentration with the backscatter diagnostic (as opposed to imaging, which provides direct single-shot density measurements).

4. CONSIDERATIONS FOR FURTHER APPLICATION

A. Radiation Detection at Standoff Distances 10–100 m

Based on the results of the present experiment, any laser focal geometry used for remote detection at range will require peak intensities above the threshold of 1.5 TW/cm^2. Breakdowns leading to a backscatter signal with SNR >10 require higher intensities ~1.6–1.8 TW/cm^2. For example, detection at a range of 100 m using a $\lambda = 3.9$ μm, 50 ps pulse would require focusing of ~75 mJ at $f/100$ by a 1 m diameter optic. This would probe a focal volume $\sim 10^{-3}$ cm^3, providing sensitivity to seed ion densities $\sim 10^3$ – 10^4 cm^{-3} (with statistical variations in time advance below 10^4 cm^{-3} and saturation above it). This energy estimate, as well as the threshold intensity measured, is ~2 times higher than the value reported in our previous work [21] due to an uncorrected saturation in the mid-IR camera (FLIR InSb array), which led to inaccurate focal spot measurements in that experiment.

While this scaling is in principle straightforward, propagation and focusing over tens of meters is complicated by turbulence and nonlinear propagation. While the present experiment could readily be extended to distances of ~10 m, longer distances would require addressing these issues. We note that delivering intense pulses at range through realistic atmospheric conditions is an active area of theoretical research [46], and that a recent experiment has demonstrated long-range propagation by self-channeling through turbulence and linear compensation of initial pulse chirp [47,48].

Also, as noted above, 2%–3% of all shots exhibited very bright, early breakdowns with large values of time advance, uncorrelated with the radioactive source or the driving intensity. This behavior is consistent with dust-initiated avalanches, which have a reduced breakdown threshold and start at high local density. While these breakdowns would be an important consideration in the field, it is easy to filter them from the data owing to their large time advance (30–40 ps) and high relative backscatter energy compared to O_2^- ion-seeded breakdowns (10–20 ps time advance). However, in a detection environment that includes enough dust and aerosols to seed such early breakdowns on every shot, additional filtering of the data would be required. One possibility would be to combine information from multiple detection channels (backscatter time, total backscatter amount, visible plasma imaging to determine seed distribution) to further constrain data processing.

While increasing the focal volume at a fixed seed density increases the number of breakdown sites, the laser pulse repetition rate can be severely limited by the much longer diffusion time of long-lived breakdown products out of larger focal volumes, lengthening the time required for air to return to equilibrium conditions. The presence in the focal volume of seed ions produced not by the radioactive source, but by the prior laser pulse, is to be avoided. This issue will become more pronounced at standoff distances where focal volumes might increase by a few orders of magnitude. However, in a remote detection environment, this self-seeding effect might be avoided by dynamically sweeping the focal position.

Although, for the experiment results presented in this paper, we used an $f/80$ lens to collect backscattered mid-IR spectra, we still observed a detectable signal when this lens was removed ($> f/1000$ effective collection set by the spectrometer entrance slit), albeit with a much lower SNR (SNR < ~10). While this configuration would be ready for use at range with our current laser energy and pulse duration, it would depend more sensitively on the absolute backscatter.

Increasing the laser focusing beyond $f/100$ quickly leads to a very large focal volume due to its characteristic w_0^4 scaling, and, correspondingly, sensitivity is degraded, as the focal volume will always contain many seed ions even at background conditions (negative ion densities of $\sim 10^2$ – 10^3 cm^{-3}). Providing the seed ion density exceeds background levels, maintaining sensitivity

requires either decreasing the effective volume probed or decreasing the number of ions from which seed electrons are liberated. The first scenario could be achieved by using a longer wavelength laser, such that higher-order MPI from negative ions effectively shrinks the probed volume. In the second scheme, a separate, low-power near-IR beam is focused to a smaller focal volume to pre-ionize only a portion of the negative ions [20], after which a long-wavelength pulse drives an avalanche.

In the present experiment, we inferred time advances using a limited spectral range ($\lambda = 3.6$–3.8 μm), even though the spectrometer had considerably more resolving power. Temporal resolution of the breakdown in an integrated system could be increased by matching the spectral range of the spectrometer to the expected time advance, or adjusting the chirp of the beam to increase the variation in wavelength over the time interval of interest.

B. Measurements of Extremely Low Charge Densities

In the present paper, we have demonstrated direct measurement of an extremely low density (10^5 cm^{-3} and below) of a specific charged species, O_2^-, and possibly other ions produced through subsequent air chemistry. This capability is a large improvement over other methods, such as microwave and optical diagnostics [29,30] and plasma conductivity measurements [31], which are limited to much higher charge densities ($> \sim 10^{10}$ cm^{-3}), often require large volumes or integration lengths, and are difficult to absolutely calibrate. While other charged particle diagnostics (such as the Gerdien ion counter used above) are able to detect small numbers of particles, they cannot easily distinguish different species, and they lack time and space resolution.

For higher seed ion densities where single seed-initiated avalanches are not resolvable, it may still be possible to determine a wide range of seed densities by observing the time advance. For a low number of seeds per volume, the time advance will be statistical, and the density can be inferred from simulations as in Fig. 5(b). As the seed density is further increased, the time advance will further increase as the high initial density of seed electrons within a single diffusion volume decreases the required growth to achieve saturation [19,20]. While this approach requires using simulations to infer the density correlated with a measured avalanche time advance, the excellent agreement between our measurements and simulations gives us confidence that we can rely on the calculated growth rates.

5. CONCLUSION

We have demonstrated laser-induced avalanche detection of a radioactive source in true standoff geometry, where the three remote detection channels rely only on backscattering or plasma emission. Of the three demonstrated detection channels, we found that the breakdown time advance diagnostic—which depends on single-shot spectrally resolved measurements of chirped pulse backscatter—gave the most precise measure of the radiation environment, and was also immune to pump laser scattering by multiple breakdown plasma sites.

We have also demonstrated that direct imaging of the laser breakdown volume, which enables counting of the individual breakdown plasma sites and measuring their sizes, is a very powerful benchmark for assessing the fidelity of the three remote detection channels. The direct imaging measurement also makes possible the absolute determination of extremely low-charge densities, a technique of interest to a wide range of applications.

Funding. Defense Threat Reduction Agency (DTRA) (HDTRA11510002); Air Force Office of Scientific Research (AFOSR) (FA9550-16-10121, FA9550-16-10259); Office of Naval Research (ONR) (N00014-17-1-2705); NNSA SSGF program (DE-NA0003864).

Acknowledgment. The authors thank J. Isaacs and P. Sprangle for help in improving diffusion calculations and updating rate coefficients for the simulations. We also thank C. Winstead for useful discussions on radiation-induced air chemistry. D.W. acknowledges support from the NNSA SGF program (DE-NA0003864).

See Supplement 1 for supporting content.

REFERENCES

1. K. P. Ziock, W. W. Craig, L. Farbis, R. C. Lanza, S. Gallagher, B. K. P. Horn, and N. W. Madden, "Large area imaging detector for long-range, passive detection of fissile material," IEEE Trans. Nucl. Sci. **51**, 2238–2244 (2004).
2. M. V. Hynes, M. Toolin, B. Harris, J. McElroy, M. S. Wallace, L. J. Schultz, M. Galassi, A. Hoover, M. Mocko, D. Palmer, S. Tornga, D. Wakeford, H. R. Andrews, E. T. H. Clifford, L. Li, N. Bray, D. Locklin, R. Lanza, B. Horn, and D. Wehe, "The Raytheon-SORDS trimordal imager," Proc. SPIE **7310**, 731003 (2009).
3. S. Zelakiewicz, R. Hoctor, A. Ivan, W. Ross, E. Nieters, W. Smith, D. McDevitt, M. Wittbrodt, and B. Milbrath, "SORIS—a standoff radiation imaging system," Nucl. Instrum. Methods Phys. Res. A **652**, 5–9 (2011).
4. R. Pöllänen, H. Toivonen, K. Peräjärvi, T. Karhunen, T. Ilander, J. Lehtinen, K. Rintala, T. Katajainen, J. Niemelä, and M. Juusela, "Radiation surveillance using an unmanned aerial vehicle," Appl. Radiat. Isot. **67**, 340–344 (2009).
5. X. B. Tang, J. Meng, P. Wang, Y. Cao, X. Huang, L. S. Wen, and D. Chen, "Efficiency calibration and minimum detectable activity concentration of a real-time UAV airborne sensor system with two gamma spectrometers," Appl. Radiat. Isot. **110**, 100–108 (2016).
6. T. Hinterhofer, M. Pfennigbauer, A. Ullrich, D. Rothbacher, S. Schraml, and M. Hofstätter, "UAV-based lidar and gamma probe with real-time data processing and downlink for survey of nuclear disaster locations," Proc. SPIE **10629**, 106290C (2018).
7. R. J. Nemzek, J. S. Dreicer, D. C. Torney, and T. T. Warnock, "Distributed sensor networks for detection of mobile radioactive sources," IEEE Trans. Nucl. Sci. **51**, 1693–1700 (2004).
8. F. Ding, G. Song, K. Yin, J. Li, and A. Song, "A GPS-enabled wireless sensor network for monitoring radioactive materials," Sens. Actuators A Phys. **155**, 210–215 (2009).
9. J. R. Wachter and D. A. Cremers, "Determination of uranium in solution using laser-induced breakdown spectroscopy," Appl. Spectrosc. **41**, 1042–1048 (1987).
10. J. P. Singh, F. Y. Yueh, H. Zhang, and K. P. Karney, "A preliminary study of the determination of uranium, plutonium and neptunium by laser-induced breakdown spectroscopy," Rec. Res. Dev. Appl. Spectrosc. **2**, 59–67 (1999).
11. J. P. Singh and S. N. Thakur, *Laser Induced Breakdown Spectroscopy* (Elsevier, 2007).
12. S. S. Nabiev and L. A. Palkina, "Current trends in the development of remote methods of detecting radioactive and highly toxic substances," in *The Atmosphere and Ionosphere*, V. L. Bychkov, G. V. Golubkov, and A. I. Nikitin, eds. (Springer, 2014), pp. 113–200.
13. J. M. Dai, X. F. Lu, J. Liu, I. C. Ho, N. Karpowicz, and X.-C. Zhang, "Remote THz wave sensing in ambient atmosphere," Terahertz Sci. Technol. **2**, 131–143 (2009).

14. Y. F. Su, R. G. Tonkyn, L. E. Sweet, J. F. Corbey, S. A. Bryan, and T. J. Johnson, "Characterization of uranium ore concentrate chemical composition via Raman spectroscopy," Proc. SPIE **10629**, 106290G (2018).
15. O. Katz, A. Natan, Y. Silberberg, and S. Rosenwaks, "Standoff detection of trace amounts of solids by nonlinear Raman spectroscopy using shaped femtosecond pulses," Appl. Phys. Lett. **92**, 171116 (2008).
16. A. S. Grishkanich, V. G. Bespalov, S. K. Vasiev, A. S. Gusarov, S. V. Kascheev, V. V. Elizarov, and A. P. Zhevlakov, "Monitoring radioactive contamination by hyperspectral lidar," Proc. SPIE **9486**, 94860X (2015).
17. E. Puckrin and J. M. Thériault, "Passive standoff detection of radiological products by Fourier-transform infrared radiometry," Opt. Lett. **29**, 1375–1377 (2004).
18. V. L. Granatstein and G. S. Nusinovich, "Detecting excess ionizing radiation by electromagnetic breakdown of air," J. Appl. Phys. **108**, 063304 (2010).
19. P. Sprangle, B. Hafizi, H. M. Milchberg, G. Nusinovich, and A. Zigler, "Active remote detection of radioactivity based on electromagnetic signatures," Phys. Plasmas **21**, 013103 (2014).
20. J. Isaacs, C. Miao, and P. Sprangle, "Remote monostatic detection of radioactive material by laser-induced breakdown," Phys. Plasmas **23**, 033507 (2016).
21. R. M. Schwartz, D. Woodbury, J. Isaacs, P. Sprangle, and H. M. Milchberg, "Remote detection of radioactive material using mid-IR laser-driven electron avalanche," Sci. Adv. **5**, eaav6804 (2019).
22. G. S. Nusinovich, P. Sprangle, C. A. Romero-Talamas, and V. L. Granatstein, "Range, resolution and power of THz systems for remote detection of concealed radioactive materials," J. Appl. Phys. **109**, 083303 (2011).
23. Y. S. Dimant, G. S. Nusinovich, P. Sprangle, J. Penano, C. A. Romero-Talamas, and V. L. Granatstein, "Propagation of gamma rays and production of free electrons in air," J. Appl. Phys. **112**, 083303 (2012).
24. G. S. Nusinovich, "Remote detection of concealed radioactive materials by using focused powerful terahertz radiation," J. Infrared Millim. Terahertz Waves **37**, 515–535 (2016).
25. D. Kim, D. Yu, A. Sawant, M. S. Choe, I. Lee, S. G. Kim, and E. Choi, "Remote detection of radioactive material using high-power pulsed electromagnetic radiation," Nat. Commun. **8**, 15394 (2017).
26. D. Woodbury, J. Wahlstrand, A. Goers, L. Feder, B. Miao, G. Hine, F. Salehi, and H. Milchberg, "Single-shot measurements of laser-induced avalanche breakdown demonstrating spatial and temporal control by an external source," in *58th Annual Meeting of the American Physical Society Division of Plasma Physics* (APS, 2016), presentation CP10.00154.
27. M. L. Huertas, J. Fontan, and J. Gonzalez, "Evolution times of tropospheric negative ions," Atmos. Environ. **12**, 2351–2362 (1967).
28. F. F. Chen, *Introduction to Plasma Physics and Controlled Fusion* (Plenum, 1984).
29. Z. Zhang, M. N. Shneider, and R. B. Miles, "Microwave diagnostics of laser-induced avalanche ionization in air," J. Appl. Phys. **100**, 074912 (2006).
30. Y.-H. Chen, S. Varma, T. M. Antonsen, and H. M. Milchberg, "Direct measurement of the electron density of extended femtosecond laser pulse-induced filaments," Phys. Rev. Lett. **105**, 215005 (2010).
31. D. Abdollahpour, S. Suntsov, D. G. Papazoglou, and S. Tzortzakis, "Measuring easily electron plasma densities in gases produced by ultrashort lasers and filaments," Opt. Express **19**, 16866–16871 (2011).
32. G. Andriukaitis, T. Balčiūnas, S. Ališauskas, A. Pugžlys, A. Baltuška, T. Popmintchev, M.-C. Chen, M. M. Murnane, and H. C. Kapteyn, "90 GW peak power few-cycle mid-infrared pulses from an optical parametric amplifier," Opt. Lett. **36**, 2755 (2011).
33. N. M. Kroll and K. M. Watson, "Multiphoton detachment of negative ions," DARPA Final Technical Report JSR-73-6 (1974).
34. V. A. Mohnen, "Discussion of the formation of major positive and negative ions up to the 50 km level," Pure Appl. Geophys. **84**, 141–151 (1971).
35. M. L. Huertas and J. Fontan, "Formation of stable positive and negative small ions of tropospheric interest," Atmos. Environ. **16**, 2521–2527 (1982).
36. J. C. Rienstra-Kiracofe, G. S. Tschumper, H. F. Schaefer III, S. Nandi, and G. B. Ellison, "Atomic and molecular electron affinities: photoelectron experiments and theoretical calculations," Chem. Rev. **102**, 231–282 (2002).
37. J. Way, J. Hummelt, and J. Scharer, "Experimental measurements of multiphoton enhanced air breakdown by a subthreshold intensity excimer laser," J. Appl. Phys. **106**, 083303 (2009).
38. G. S. Nusinovich, F. Qiao, D. G. Kashyn, R. Pu, and L. S. Dolin, "Breakdown-prone volume in terahertz wave beams," J. Appl. Phys. **113**, 233303 (2013).
39. National Institute of Standards and Technology, http://physics.nist.gov/PhysRefData/Star/Text/ASTAR.html.
40. P. Polynkin and J. V. Moloney, "Optical breakdown of air triggered by femtosecond laser filaments," Appl. Phys. Lett. **99**, 151103 (2011).
41. V. V. Apollonov, L. M. Vasilyak, S. Yu. Kazantsev, I. G. Kononov, D. N. Polyakov, A. V. Saifulin, and K. N. Firsov, "Electric-discharge guiding by a continuous spark by focusing CO_2-laser radiation with a conic mirror," Quantum Electron. **32**, 115–120 (2002).
42. K. Mansour, M. J. Soileau, and E. W. Van Stryland, "Nonlinear optical properties of carbon-black suspensions," J. Opt. Soc. Am. B **9**, 1100–1109 (1992).
43. J. D. Huba, "Weakly ionized plasmas," in *NRL Plasma Formulary Supported by The Office of Naval Research* (Naval Research Laboratory, 2013), p. 39.
44. A. W. Ali, "Electron energy loss rates in N2, O2, and air," NRL Memorandum Report 5400 (1984).
45. J. Isaacs, D. Woodbury, and P. Sprangle, "Remote detection of radioactive material using optically induced air breakdown ionization," Proc. SPIE **11010**, 110101E (2019).
46. J. Peñano, J. P. Palastro, B. Hafizi, M. H. Helle, and G. P. DiComo, "Self-channeling of high-power laser pulses through strong atmospheric turbulence," Phys. Rev. A **96**, 013829 (2017).
47. M. H. Helle, G. DiComo, J. Palastro, J. Peñano, J. Elle, and A. Schmitt-Sody, "Nonlinear self-channeling of laser pulses through distributed atmospheric turbulence," in *Frontiers in Optics*, OSA Technical Digest (online) (Optical Society of America, 2017), paper JTu3A.59.
48. G. P. DiComo, "Nonlinear self-channeling of high-power lasers through turbulent atmospheres," Doctoral Dissertation (University of Maryland, 2018).